

Super-Resolution Imaging of Clickable Graphene Nanoribbons Decorated with Fluorescent Dyes

Dharati Joshi,^{†,‡} Meghan Hauser,^{†,‡} Gregory Veber,[†] Alexandra Berl,[†] Ke Xu,^{*,†,‡,§} and Felix R. Fischer^{*,†,§,||}

[†]Department of Chemistry, University of California, Berkeley, California 94720, United States

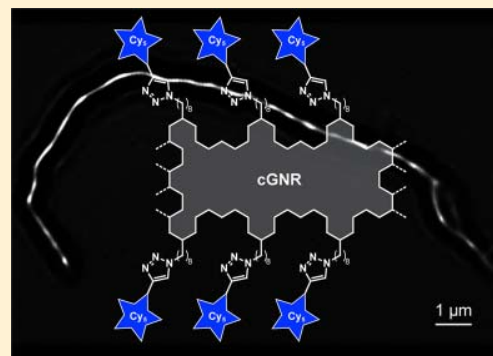
[‡]Division of Molecular Biophysics and Integrated Bioimaging, Lawrence Berkeley National Laboratory, Berkeley, California 94720, United States

[§]Materials Sciences Division, Lawrence Berkeley National Laboratory, Berkeley, California 94720, United States

^{||}Kavli Energy NanoSciences Institute at the University of California Berkeley and the Lawrence Berkeley National Laboratory, Berkeley, California 94720, United States

Supporting Information

ABSTRACT: The functional integration of atomically defined graphene nanoribbons (GNRs) into single-ribbon electronic device architectures has been limited by access to nondestructive high-resolution imaging techniques that are both compatible with common supports such as Si or Si/SiO₂ wafers and capable of resolving individual ribbons in dilute samples. Conventional techniques such as scanning probe (AFM, STM) or electron microscopy (SEM, TEM) have been restricted by requisite sample preparation techniques that are incompatible with lithographic device fabrication. Here we report the design and synthesis of ultralong (~10 μm) cove-type GNRs (cGNRs) featuring azide groups along the edges that can serve as a universal handle for late-stage functionalization with terminal alkynes. Copper-catalyzed click-chemistry with Cy5 fluorescent dyes gives rise to cGNRs decorated along the edges with fluorescent tags detectable by optical microscopy. The structures of individual dye-functionalized cGNRs spin-coated from a dilute solution onto transparent and opaque insulating substrates were resolved using diffraction-limited fluorescence microscopy and super-resolution microscopy (SRM) imaging techniques. Analysis of SRM images reveals an apparent width of cGNRs in the range 40–50 nm and lengths in excess of 10 μm, the longest GNRs imaged to date. Isolated cGNRs can even be distinguished from bundles and larger aggregates as long as the center-to-center distance is greater than the apparent width.



INTRODUCTION

While narrow graphene nanoribbons (GNRs) share many of the unusual electronic properties of two-dimensional graphene, the lateral quantum confinement imposed by their finite width (<2 nm) opens a sizable electronic band gap, elevating GNRs to a privileged position as a functional material for high-performance electronic device applications.¹ The intrinsic band gap of GNRs is tunable and is intimately linked to the width^{2–5} and crystallographic symmetry of the ribbon.^{2,3,6} Any rational approach to tailoring the band structure of GNRs requires atomically precise control over critical structural parameters such as width, length, and symmetry. As traditional top-down patterning techniques^{7–11} lack the level of control required for precise bandgap engineering, recent examples of deterministic bottom-up approaches rely on the covalent growth of GNRs from small-molecule building blocks^{12–17} in solution or on catalytic metal surfaces. While bottom-up synthesized GNRs grown on a catalytically active metal surface can be imaged with atomically resolved scanning probe microscopy (SPM),

an imaging technique capable of resolving the detailed atomic and electronic structure of individual, immobilized GNRs, these advanced tools are not scalable to bulk processing and suffer from significant drawbacks (e.g., requirement of a metallic substrate) that hamper the integration of GNRs into single-ribbon electronic devices.^{18,19} Solution-based approaches relying on either Diels-Alder or transition-metal-catalyzed Yamamoto polymerizations followed by oxidative cyclodehydrogenation reactions have yielded bulk samples of cove- and chevron-type GNRs, yet critical challenges remain toward the incorporation of solution-synthesized GNRs into device architectures such as field effect transistors (FETs).²⁰ The solution processing of GNR dispersions, for example, is limited by the inherent insolubility and the tendency of GNRs to aggregate into bundles driven by noncovalent stacking interactions along the extended π -conjugated backbone.²¹

Received: May 3, 2018

Published: July 5, 2018

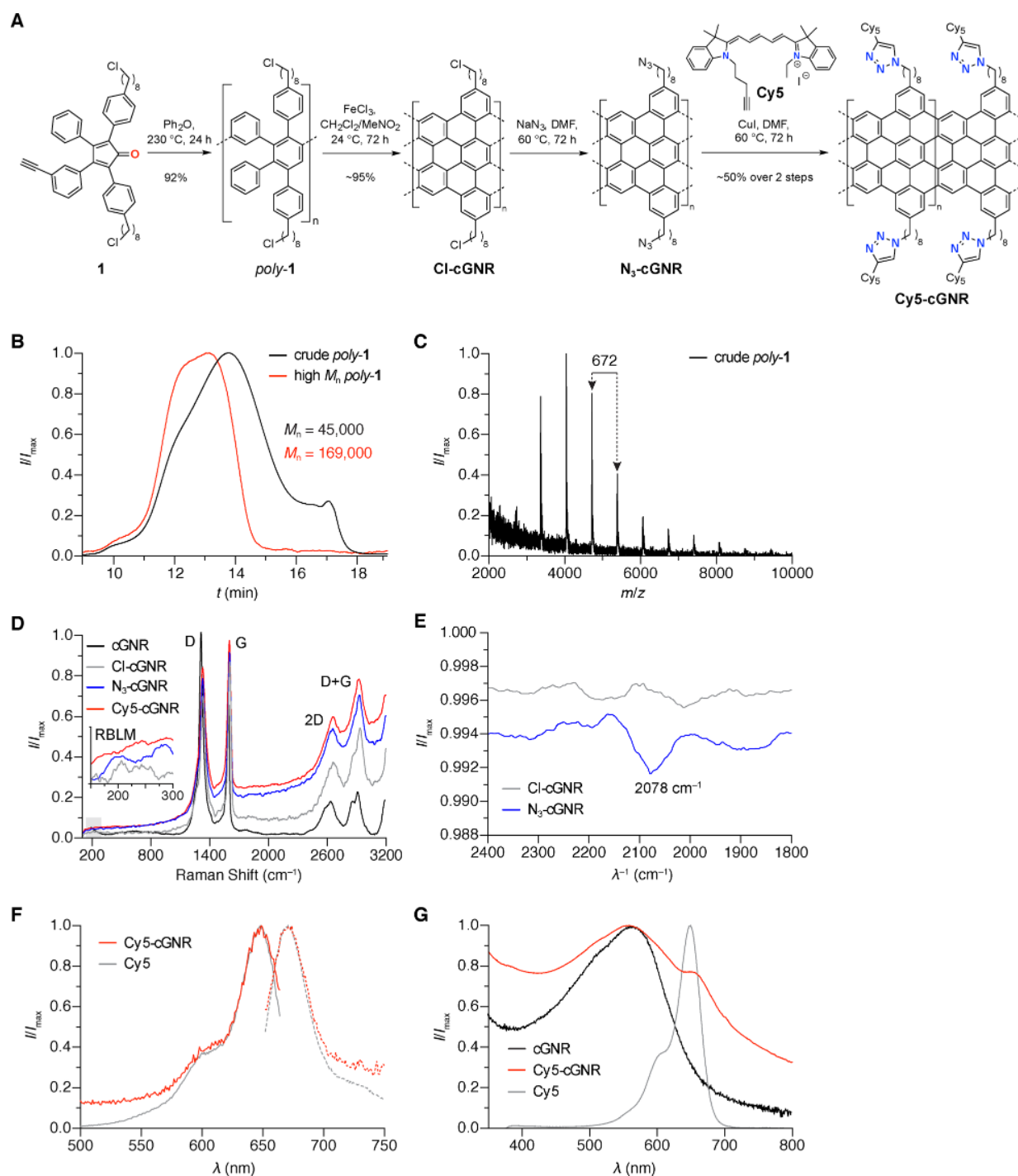


Figure 1. Synthesis and characterization of dye-functionalized Cy5-cGNRs. (A) Schematic representation of the synthesis of clickable N_3 -cGNRs and their functionalization with a Cy5 dye bearing a terminal alkyne. (B) Size exclusion chromatography (SEC) trace of crude *poly-1* (black) and the high molecular weight fraction (red) isolated by preparative SEC. (C) MALDI mass spectrum of crude *poly-1* showing the characteristic family of molecular ions. The spacing corresponds to the mass of the polymer repeat unit. (D) Raman spectrum ($\lambda_E = 514$ nm) of bulk samples of unsubstituted cGNRs, Cl-cGNRs, N_3 -cGNRs, and Cy5-cGNRs. Inset shows a magnification of the spectral region associated with the radial breathing like mode (RBLM). (E) IR spectrum of Cl-cGNRs and N_3 -cGNRs showing the characteristic peak associated with the azide stretching mode. (F) Fluorescence excitation (solid lines) and emission (dotted lines) spectra of free Cy5 and dye-functionalized Cy5-cGNRs. (G) UV-vis absorption spectra of unsubstituted cGNRs, free Cy5, and dye-functionalized Cy5-cGNRs.

While flakes of single-layer graphene can be readily visualized on SiO_2 and transparent substrates by optical microscopy,^{22,23} the spatial localization of narrow solution-processed GNRs on insulating substrates required for aligning lithographic masks

used in device fabrication remains a daunting challenge. Traditional imaging techniques such as atomic force microscopy (AFM),^{24,25} transmission electron microscopy (TEM),²⁶ scanning electron microscopy (SEM),^{25,26} and

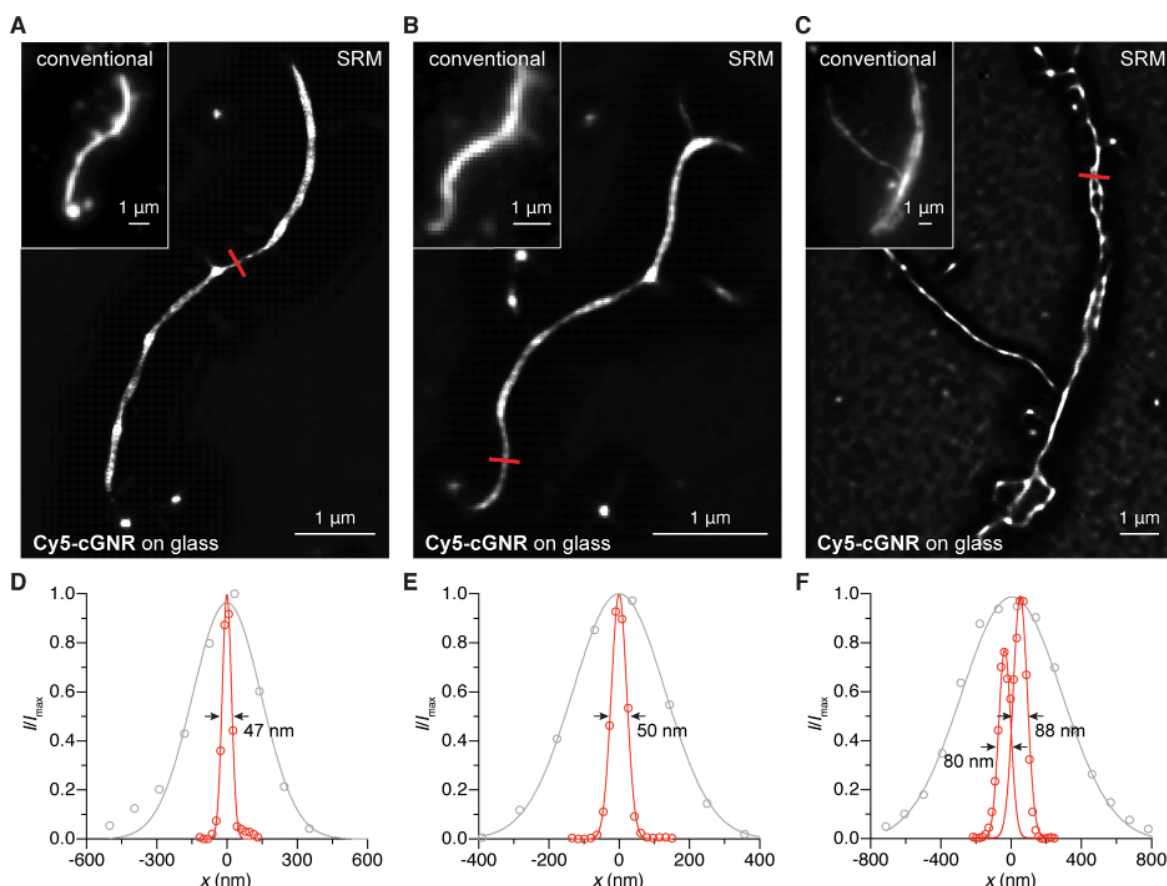


Figure 2. Comparison between conventional fluorescence and super-resolution microscopy of dye-functionalized Cy5-cGNRs. (A–C) SRM (SRRF) fluorescence images of samples of Cy5-cGNRs on silanized glass coverslips. Figure insets show conventional diffraction-limited microscopy of the same area of the sample. (D–F) Fluorescence intensity cross-section profiles at positions highlighted (red lines) in A–C in conventional diffraction-limited fluorescence microscopy (gray) and SRM (SRRF) images (red) (circles: experimental data, lines: Gaussian fits). The SRM data in (F) are fitted by two Gaussian peaks with a 98 nm peak-to-peak distance.

scanning tunneling microscopy (STM)^{12,13,24,25} are either restricted to atomically flat substrates (e.g., mica, graphite), require the sample to be suspended on a fragile, atomically thin support, or are restricted to conductive surfaces incompatible with electronic device architectures. While the lateral resolution of traditional optical microscopy is limited by the diffraction of light (~ 300 nm), recent advancements in super-resolution microscopy (SRM) have enabled subdiffraction imaging of nanoscale structures in biological specimens^{27,28} and even some selected functional materials.^{29–33}

We herein report the late-stage covalent functionalization of solution-synthesized cove-type GNRs (cGNRs) with fluorescent dyes and their optical visualization on insulating substrates using SRM. Our synthetic modification of cGNRs introduces an azide functional group in the solubilizing side chains of cGNRs that can both be conjugated to a large variety of commercial fluorescent dyes and also represents a universal linker for the covalent functionalization of GNRs through click-chemistry. A direct correlation of conventional diffraction-limited optical microscopy and SRM of Cy5-functionalized cGNRs reveals that isolated individual ribbons and even aggregates and bundles of cGNRs can be resolved down to the apparent width of ~ 40 – 50 nm.

Comparison of SRM images with AFM of a carbon nanotube reference reveals that our super-resolution techniques represent a versatile, nondestructive tool to localize

individual ribbons and even complex graphene nanostructures on insulating substrates suitable for electronic device fabrication.

RESULTS AND DISCUSSION

The solution-based bottom-up synthesis of fluorescent dye-functionalized cGNRs (Cy5-cGNR) is depicted in Figure 1A. Since neither the dye (Cy5) nor the azide group required for the click-chemistry is compatible with the harsh reaction conditions associated with the oxidative cyclodehydrogenation of the GNR precursor polymers, we designed a synthetic route around a late-stage functional group interconversion: a nucleophilic substitution of an alkyl chloride with an azide on the fully graphitized GNR. Diels–Alder polymerization and decarbonylation of cyclopentadienone **1** featuring two (8-chlorooctyl)benzene substituents yielded the polyphenylene intermediate poly-**1** in 92% yield. The molecular weight dispersity, D_M , of poly-**1** derived from size exclusion chromatography (SEC, calibrated to polystyrene standards) ranges from 2.5 to 3.9 with a number-average molecular weight M_n of 45 kg mol^{-1} (Figure 1B). Preparative SEC yielded a high molecular weight fraction of poly-**1** with $D_M = 1.7$ and an M_n of 169 kg mol^{-1} , which was carried on through the rest of the synthesis. MALDI mass spectrometry (Figure 1C) shows the characteristic family of molecular ions separated by the mass of the decarbonylated monomer **1** ($\Delta M = 672 \text{ g mol}^{-1}$).

Oxidative cyclodehydrogenation of poly-1 yields structurally homogeneous cGNRs (Cl-cGNR) featuring solubilizing 8-chlorooctyl side chains along the protrusions of the cove-edges. Raman spectroscopy ($\lambda_E = 532$ nm) shows the characteristic signatures for the radial breathing like mode (RBLM)^{16,34} (232 cm^{-1} ; fwhm = 83 cm^{-1}), the D (1334 cm^{-1} ; fwhm = 56 cm^{-1}) and G (1607 cm^{-1} ; fwhm = 26 cm^{-1}) peaks with a ratio of $I_{D/G} = 0.76$, and higher order 2D and D+G peaks (Figure 1D). Nucleophilic substitution of the primary chlorides in the solubilizing side chains of Cl-cGNR with sodium azide gave the clickable cGNRs (N_3 -cGNR). A comparison of the infrared spectra of Cl-cGNR and N_3 -cGNR (Figure 1E) reveals the appearance of a characteristic absorption peak ($\lambda^{-1} = 2078$ cm^{-1}) assigned to the azide linear stretching mode.³⁵ The Raman spectrum of N_3 -cGNR shows no significant change in the RBLM, D, and G peak position/ratio, consistent with the selective attack of the azide on the ancillary alkyl chloride side chain rather than a functionalization of the conjugated backbone of the cGNRs. Copper-catalyzed Huisgen 1,3-dipolar cycloaddition between N_3 -cGNRs and a Cy5 dye bearing a terminal alkyne gave the dye-functionalized Cy5-cGNRs in ~50% yield over two steps (determined by elemental analysis, Supporting Information Figure S1). Fluorescence and UV-vis spectroscopy show the successful integration of the dye with the cGNRs (Figure 1F,G). The fluorescence excitation and emission spectra of Cy5-cGNRs are almost indistinguishable from the spectra of free Cy5, indicating that the alkyl spacers between the dye and the extended π -system of the cGNR effectively prevent quenching of excited states. The excitation (emission) maxima are found at 649 nm (674 nm) and 648 nm (671 nm) for the Cy5-GNRs and Cy5, respectively. While free Cy5 shows a maximum UV-vis absorption at $\lambda_{\text{max}} = 650$ nm, the corresponding transition in the dye-functionalized Cy5-GNRs is slightly red-shifted and appears as a shoulder around $\lambda = 663$ nm.

Samples of dye-functionalized GNRs for fluorescence imaging were prepared by spin-coating dilute suspensions (0.1 mg mL^{-1}) of Cy5-cGNRs in acetone first onto silanized glass coverslips. Raman mapping of the G peak intensity reveals a homogeneous coverage of the surface with Cy5-cGNRs with only minimal aggregation into larger bundles (Supporting Information Figure S2). Conventional, diffraction-limited fluorescence microscopy (laser $\lambda_{\text{Ex}} = 647$ nm; 2 mW cm^{-2}) of Cy5-cGNRs on glass coverslips reveals isolated fluorescent strings and larger bundles with typical apparent lengths in the range 5–15 μm (Figure 2A–C insets). Fluorescence intensity cross-section profiles of individual Cy5-cGNRs show an apparent full width at half-maximum (fwhm) of ~300 nm (gray circles and lines in Figure 2D,E), well in agreement with the expected diffraction limit given the emission wavelength of Cy5 ($\lambda_{\text{Em}} = 671$ nm). While conventional fluorescence microscopy of Cy5-cGNRs clearly reveals the position of dye-functionalized cGNRs even on an insulating nonplanar substrate, the resolution is insufficient to unambiguously distinguish between single Cy5-cGNRs and larger bundles.

To increase the lateral resolution and to identify the number and the arrangement of cGNRs in a specific sample, we imaged the same structures using SRM. The sample slide was immersed in an imaging buffer containing 2-aminoethanethiol to assist the photoswitching/blinking of Cy5 dyes, and the laser power was increased to 2 kW cm^{-2} . Under these routine STORM (stochastic optical reconstruction microscopy) SRM

conditions,³⁶ the majority of the Cy5-dyes were expected to reside in a nonfluorescent dark state, and only the small number of emitting molecules distributed across a frame contribute to the single-molecule localization. Unexpectedly, we found that even at the highest concentration of thiol quencher (100 mM), the inherent fluorescence of the Cy5 dyes lining the edges of Cy5-cGNRs could never be entirely switched to the dark state. As a result, we observed overlapping emissions from closely localized dye molecules in imaging frames (see Supporting Information Figure S3 for representative frames) that prevented us from performing single-molecule localization analysis required for STORM. This effect is likely due to a combination of the unusually high density of dyes along the edges of the cGNR (~1–2 Cy5 dyes nm^{-1}) and the hydrophobic local environment of the cGNR that limits the local concentration of thiol quencher.

While we were unable to attain the efficient single-molecule switching required for STORM, we observed significant temporal fluorescence intensity fluctuations along the length of Cy5-cGNRs (Supporting Information Figure S3). This temporal variation of the fluorescence intensity of images collected in different frames allowed us to apply super-resolution optical fluctuation imaging (SOFI)³⁷ and super-resolution radial fluctuation (SRRF)³⁸ analysis methods. Figure 2A,B show SRRF images of the two distinct Cy5-cGNRs corresponding to the diffraction-limited images depicted in the figure insets. Intensity cross-section profiles show an apparent fwhm of 47–50 nm for both dye-functionalized cGNRs. Assuming the backbone of the cGNRs adsorbs planar and parallel to the surface, the theoretically predicted width of Cy5-cGNRs is expected to range between 7 and 10 nm. The uniform apparent width of ~50 nm observed across numerous different Cy5-cGNRs samples (see Supporting Information Figure S4 for additional images) suggests that single isolated Cy5-cGNRs can be resolved with an apparent width close to the reported theoretical resolution limit of SRRF.³⁸ An analysis of multiple images of dye-functionalized cGNRs suggests that it is not unusual for single ribbons to reach lengths of 6–10 μm corresponding to 8000–12 000 linearly fused monomer units, the longest bottom-up synthesized GNRs reported to date.^{16,25,39}

SRRF imaging of dye-functionalized Cy5-cGNRs not only represents a ~10-fold improvement over the resolution of diffraction-limited fluorescence microscopy images (Figure 2A–C insets) but further provides a reliable tool to analyze structures composed of entangled cGNR bundles and potentially even more complex functional arrays. Figure 2C shows both a conventional fluorescence image and a SRRF image of a Cy5-cGNR bundle composed of entangled cGNRs. The fluorescence intensity cross-section profile for a region of the diffraction-limited image shows a single unresolved broad peak with an fwhm of 670 nm. In contrast, the corresponding SRRF image reveals two parallel cGNRs. The intensity cross-section profile shows two well-separated peaks at 98 nm center-to-center distance with fwhm's of 80 and 88 nm, respectively. This example demonstrates that SRRF imaging of dye-functionalized GNRs can resolve structural details well below the resolution limit imposed by the diffraction of light.

In an effort to corroborate the apparent width of Cy5-cGNRs derived from SRRF analysis to the real dimensions of the ribbon, we selected single-wall carbon nanotubes (SWNTs) as a reference standard that could be independently

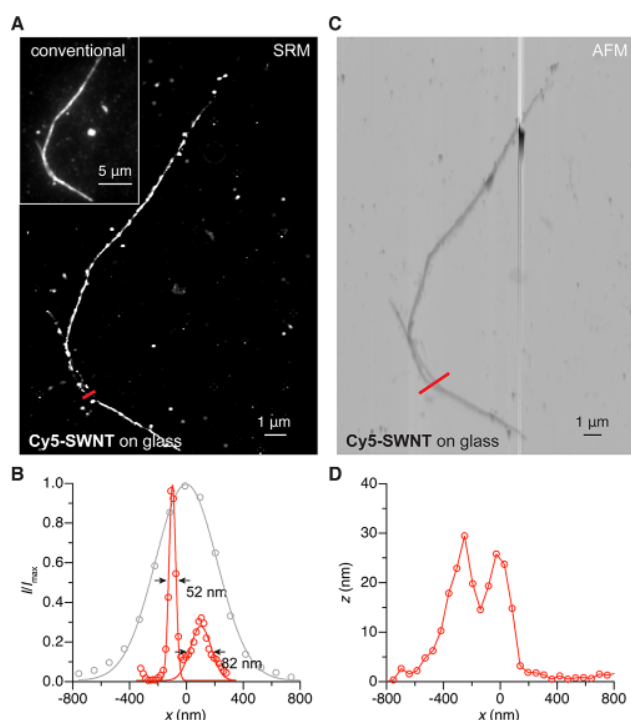


Figure 3. Conventional fluorescence, super-resolution, and atomic force microscopy of dye-functionalized Cy5-SWNTs. (A) SRM (SRRF) fluorescence image of Cy5-SWNTs on a glass coverslip. Figure inset shows conventional diffraction-limited microscopy of the same area of the sample. (B) Fluorescence intensity cross-section profiles at positions highlighted (red lines) in A in the conventional diffraction-limited fluorescence microscopy (gray) and SRM (SRRF) (red) images (circles: experimental data, lines: Gaussian fits). (C) AFM image of the same area of the sample depicted in A. (D) AFM height profile of Cy5-SWNTs at the position highlighted (red line) in C.

verified by AFM (we were unable to resolve cGNRs on glass directly, as the surface roughness of glass coverslips is greater than the apparent height of individual graphene nanoribbons). Covalent functionalization of SWNTs with (2-azidoethoxy)-

benzene followed by copper-catalyzed Huisgen 1,3-dipolar cycloaddition with N-pentynyl-Cy5 gave the corresponding dye-functionalized SWNTs (Cy5-SWNT, Supporting Information Figure S5). Figure 3A shows conventional fluorescence and SRRF microscopy images of Cy5-SWNTs spin-coated from a dilute solution onto glass coverslips. The fluorescence intensity cross-section profile reveals an apparent width of 52–82 nm for individual carbon nanotubes. Analogous to our studies on Cy5-cGNRs, nanotubes within larger aggregates or bundles can be resolved by SRRF when separated by distances greater than the apparent width of a Cy5-SWNT (Figure 3A,B). A correlation of Cy5-SWNT structures imaged by SRM with AFM height profiles recorded at the same position (Figure 3C,D) reveals that the ~ 50 nm wide features resolved in our SRRF SRM images indeed correspond to individual SWNTs.

While nondestructive SRM imaging of dye-functionalized cGNRs and SWNTs on glass coverslips serves as a proof of concept, the greater challenge lies in transferring this tool to more relevant substrates such as bare Si or Si/SiO₂ wafers traditionally used in electronic device fabrication. SRM imaging on these opaque substrates was achieved by inverting the sample geometry and imaging through an opposing coverslip. Representative images of linear strings and small bundles of Cy5-cGNRs spin-coated from solution onto silanized Si and Si/SiO₂ wafers are depicted in Figure 4A,B and Figure 4C,D, respectively. Fluorescence intensity cross-section profiles of SRRF images on both bare Si and SiO₂ show an fwhm of 60–68 nm (Supporting Information Figure S6), reminiscent of the apparent width of Cy5-cGNRs on glass slides. This work demonstrates that SRM (SRRF) of dye-functionalized cGNRs can be used as a nondestructive, high-throughput, high-resolution imaging tool to localize individual isolated ribbons in the very dilute samples required for the targeted deposition of lithographic contacts in the fabrication of experimental electronic device architectures.

CONCLUSION

In conclusion, we have developed a solution-based synthesis of a new class of cGNRs functionalized with reactive azide groups

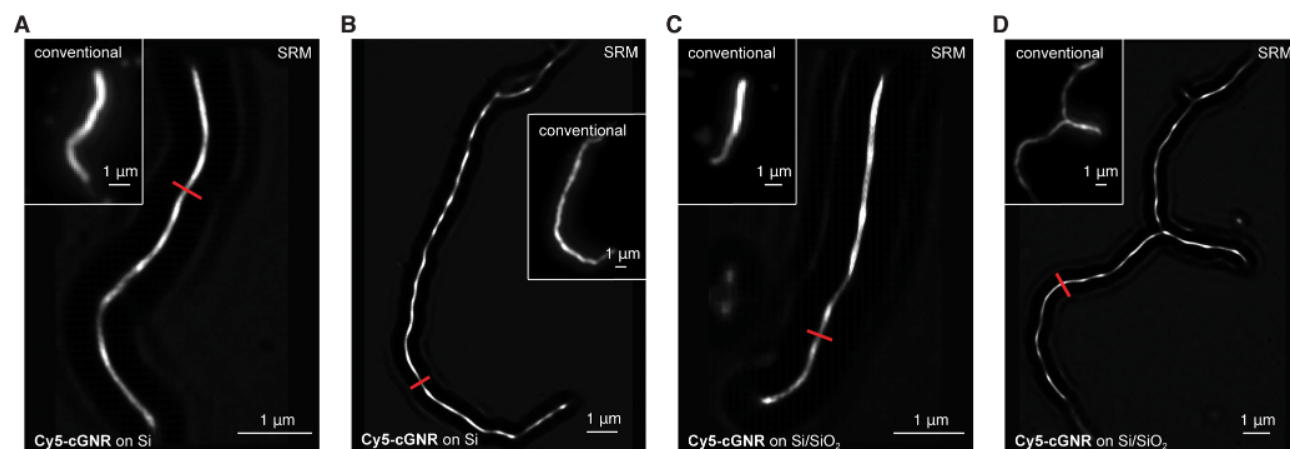


Figure 4. Comparison between conventional fluorescence and super-resolution microscopy of dye-functionalized Cy5-cGNRs on Si and Si/SiO₂ wafers. (A, B) SRM (SRRF) fluorescence images of samples of Cy5-cGNRs on silanized Si wafers. Figure insets show the conventional diffraction-limited microscopy of the same area of the sample. (C, D) SRM (SRRF) fluorescence images of samples of Cy5-cGNRs on silanized Si/SiO₂ wafers (SiO₂ thickness ~ 300 nm). Figure insets show the conventional diffraction-limited microscopy of the same area of the sample. Red lines mark the position of the cross-section profiles in Supporting Information Figure S6.

along the edges that can undergo Cu-catalyzed click-reactions with a wide variety of functional groups and molecules bearing a terminal alkyne. We have demonstrated that conjugation of these clickable cGNRs with fluorescent dyes derived from Cy5 allows the imaging of dilute dispersions of cGNRs spin-coated onto glass, Si, or Si/SiO₂ substrates using not only conventional fluorescence but also super-resolution microscopy. While the apparent width of individual ribbons imaged by SRM is well below the diffraction limit of light and allows the unambiguous distinction between isolated ribbons and larger bundles on the surface, a statistical analysis of the length of Cy5-cGNRs reveals that the exceptionally efficient Diels–Alder polymerization of cGNR monomers can give rise to graphene nanoribbons ranging in length from 6 to 10 μm . This work not only describes the development of a highly versatile and modular material based on azide-functionalized GNRs but also demonstrates that one of the critical challenges in the exploration and exploitation of the exotic properties of GNRs in electronic devices, the nondestructive imaging of dilute samples on opaque dielectric substrates, can be accomplished using super-resolution fluorescence imaging techniques derived from cell biology.

■ EXPERIMENTAL SECTION

Materials and General Methods. Unless otherwise stated, all manipulations of air- and/or moisture-sensitive compounds were carried out in oven-dried glassware, under an atmosphere of N₂. All solvents and reagents were purchased from Alfa Aesar, Spectrum Chemicals, Acros Organics, TCI America, and Sigma-Aldrich and were used as received unless otherwise noted. Organic solvents were dried by passing through a column of alumina and were degassed by vigorous bubbling of N₂ or Ar through the solvent for 20 min. Flash column chromatography was performed on SiliCycle silica gel (particle size 40–63 μm). Thin-layer chromatography was performed using SiliCycle silica gel 60 Å F-254 precoated plates (0.25 mm thick) and visualized by UV absorption. All ¹H and ¹³C NMR spectra were recorded on Bruker AVB-400, AVQ-400, and AV-600 MHz spectrometers and are referenced to residual solvent peaks (CDCl₃ ¹H NMR = 7.26 ppm, ¹³C NMR = 77.16 ppm; CD₂Cl₂ ¹H NMR = 5.32 ppm, ¹³C NMR = 54.00 ppm). ESI mass spectrometry was performed on a Finnigan LTQFT (Thermo) spectrometer in positive ionization mode. MALDI mass spectrometry was performed on a Voyager-DE PRO (Applied Biosystems Voyager System 6322) in positive mode using a matrix of dithranol. Elemental analysis (CHN) was performed on a PerkinElmer 2400 Series II combustion analyzer. Gel permeation chromatography (GPC) was performed on a LC/MS Agilent 1260 Infinity set up with one guard and two Agilent Polypore 300 \times 7.5 mm columns at 35 $^{\circ}\text{C}$. All GPC analyses were performed on a 0.2 mg/mL solution of polymer in chloroform. An injection volume of 25 μL and a flow rate of 1 mL min^{−1} were used. Calibration was based on narrow polydispersity polystyrene standards ranging from $M_w = 100$ to 4 068 981 g mol^{−1}. Infrared spectroscopy was performed on a Bruker ALPHA ATR-FTIR. Raman spectroscopy was performed on a Renishaw inVia spectrometer with a 514 nm excitation laser. Raman mapping was performed on a Horiba Jobin Yvon LabRAM ARAMIS confocal Raman microscope with a 532 nm excitation wavelength.

Preparation of Poly-1. A 10 mL Schlenk flask was charged under N₂ with **1** (45.3 mg, 0.0645 mmol) in Ph₂O (0.042 mL). The reaction mixture was degassed by three freeze–pump–thaw cycles. The reaction mixture was stirred at 230 $^{\circ}\text{C}$ for 24 h. The reaction mixture was diluted with MeOH, and the precipitate was collected via centrifugation. The solid residue was dissolved in tetrahydrofuran (THF), triturated with MeOH, and collected via centrifugation to yield poly-1 (39.9 mg, 92%) as a colorless solid. The crude polymers were fractionated by preparative GPC. ¹H NMR (400 MHz, CH₂Cl₂,

22 $^{\circ}\text{C}$): δ = 7.18–6.19 (m, 18H), 3.52 (t, J = 6.1 Hz, 4H), 2.68–2.30 (m, 4H), 1.81–1.68 (m, 4H), 1.64–1.08 (m, 20H) ppm.

Preparation of Cl-cGNR. A 500 mL Schlenk flask was charged under N₂ with poly-1 (10.5 mg) in CH₂Cl₂ (80 mL). A suspension of FeCl₃ (212 mg, 1.31 mmol, 7 equiv for each hydrogen to be removed) in MeNO₂ (4 mL) was added. The reaction mixture was stirred at 24 $^{\circ}\text{C}$ for 72 h under a continuous stream of N₂. The reaction mixture was quenched with MeOH and filtered. Washing the precipitate with MeOH (500 mL), 1 M HCl (300 mL), H₂O (1000 mL), and THF (500 mL) yielded Cl-cGNR as a black powder (10.3 mg, 95%). Raman (powder): 1334, 1607, 2654, 2937 cm^{−1}.

Preparation of N₃-cGNR. A 25 mL vial was charged with Cl-cGNR (10.6 mg) in dimethylformamide (DMF) (20 mL). The reaction mixture was sonicated for 1.5 h under N₂. NaN₃ (500 mg, 7.69 mmol) was added, and the reaction mixture was sonicated for 30 min. The reaction mixture was stirred at 60 $^{\circ}\text{C}$ for 18 h under N₂. The reaction mixture was sonicated for 4 h and stirred at 60 $^{\circ}\text{C}$ for an additional 18 h under N₂. The reaction mixture was sonicated for 1 h and filtered. Washing the precipitate with H₂O (1000 mL) and THF (500 mL) yielded N₃-cGNR as a black powder (10.8 mg). Raman (powder): 1329, 1607, 2657, 2934 cm^{−1}.

Preparation of Cy5-cGNR. A 25 mL vial was charged with N₃-cGNR (5.5 mg), N-pentynyl-Cy5 (21.1 mg, 0.0375 mmol), and CuI (60 mg, 0.315 mmol) in DMF (20 mL). The reaction mixture was sonicated for 2 h and stirred at 60 $^{\circ}\text{C}$ for 18 h under N₂. The reaction mixture was sonicated for 2 h and stirred for an additional 18 h under N₂. The reaction mixture was sonicated for 2 h and filtered. The precipitate was washed with acetone (1000 mL), MeOH (1000 mL), H₂O (500 mL), DMF (300 mL), CH₂Cl₂ (300 mL), and THF (500 mL) until the filtrate was colorless/nonfluorescent to yield Cy5-cGNR as a black powder (8.5 mg). Raman (powder): 1329, 1604, 2672, 2928 cm^{−1}; Anal. Calcd for (C₁₀₈H₁₀₈I₂N₁₀)_{*n*}: C, 72.07; H, 6.05; N, 7.78. Found: C, 43.81; H, 5.82; N, 3.63.

Sample Preparation and Imaging. Cy5-cGNRs were dispersed in acetone at 0.1 mg mL^{−1} by probe sonication for 30 min and subsequently spin-coated at 5000 rpm onto glass coverslips and silicon wafers with and without a 300 nm thick thermal oxide layer functionalized with chlorotrimethylsilane (Alfa Aesar A13651). Cy5-SWNTs were dispersed at 0.1 mg mL^{−1} in deionized water by probe sonication for 30 min and then spin-coated at 5000 rpm onto unfunctionalized glass coverslips. The samples were then mounted onto a glass slide with a Tris-Cl imaging buffer (pH 7.5) containing 100 mM 2-aminoethanethiol, 5% glucose, 0.8 mg mL^{−1} glucose oxidase, and 40 μg mL^{−1} catalase. Epifluorescence microscopy and SRM imaging were performed on a home-built setup based on a Nikon Eclipse Ti-E inverted optical microscope using an oil-immersion objective (Nikon CFI Plan Apochromat λ 100 \times , numerical aperture = 1.45) with additional 1.5 \times magnification on the microscope. A laser at 647 nm (MPB Communications) was coupled into an optical fiber after an acousto-optic tunable filter and then introduced into the sample through the back focal plane of the objective via a dichroic mirror (ZT640rdc, Chroma). Using a translation stage, the laser beam was shifted toward the edge of the objective so that emerging light reached the sample at an incidence angle close to the critical angle of the glass–water interface to achieve total internal reflection. Continuous illumination of a 647 nm laser was used to excite fluorescence from Cy5 molecules. Emission was filtered by a long-pass (ET655lp, Chroma) and a band-pass (ET700/75m, Chroma) filter and recorded with an EM-CCD (electron-multiplying charge-coupled device) camera (iXon Ultra 897, Andor) at 110 frames s^{−1} for a frame size of 256 \times 256 pixels. Diffraction-limited images were first taken at typical illumination intensities of 2 mW cm^{−2}. SRM raw data were then taken at typical illumination intensities of 2 kW cm^{−2} for 20 000 frames. Super-resolution radial fluctuation analysis was performed using a published ImageJ plugin.³⁸ The algorithm was temporal radially autocumulant order 2 (TRAC2), and optimized parameters were a ring radius of 0.5, radially magnification of 6, 6 axes in a ring, with intensity weighting, and without renormalization. Approximately 4000 frames were used to construct the final SRRF image.

■ ASSOCIATED CONTENT

● Supporting Information

The Supporting Information is available free of charge on the ACS Publications website at DOI: 10.1021/jacs.8b04679.

Figures of elemental analysis, Raman maps of Cy5-cGNRs on glass coverslips, SRM images of Cy5-cGNRs, characterization of Cy5-SWNTs, fluorescence intensity cross-section profiles, synthetic procedures for 1, and NMR spectra (PDF)

■ AUTHOR INFORMATION

Corresponding Authors

*xuk@berkeley.edu

*ffischer@berkeley.edu

ORCID

Ke Xu: 0000-0002-2788-194X

Felix R. Fischer: 0000-0003-4723-3111

Author Contributions

[#]D. Joshi and M. Hauser contributed equally to this work.

Notes

The authors declare no competing financial interest.

■ ACKNOWLEDGMENTS

This research was supported by the U.S. Department of Energy (DOE), Office of Science, Basic Energy Sciences (BES), under Award No. DE-SC0010409 (design, synthesis, and characterization of molecules and materials), and by STROBE, a National Science Foundation Science and Technology Center under Grant No. DMR 1548924 (SRM imaging). The Berkeley NMR Facility is supported in part by NIH Grant SRR023679A. D.J. acknowledges support through a National Science Foundation Graduate Research Fellowship under Grant No. DGE-1106400.

■ REFERENCES

- (1) Shen, H. L.; Shi, Y.; Wang, X. R. *Synth. Met.* **2015**, *210*, 109–122.
- (2) Barone, V.; Hod, O.; Scuseria, G. E. *Nano Lett.* **2006**, *6*, 2748–2754.
- (3) Nakada, K.; Fujita, M.; Dresselhaus, G.; Dresselhaus, M. S. *Phys. Rev. B: Condens. Matter Mater. Phys.* **1996**, *54*, 17954–17961.
- (4) Son, Y. W.; Cohen, M. L.; Louie, S. G. *Phys. Rev. Lett.* **2006**, *97*, 216803.
- (5) Yang, L.; Park, C. H.; Son, Y. W.; Cohen, M. L.; Louie, S. G. *Phys. Rev. Lett.* **2007**, *99*, 186801.
- (6) Fujita, M.; Wakabayashi, K.; Nakada, K.; Kusakabe, K. *J. Phys. Soc. Jpn.* **1996**, *65*, 1920–1923.
- (7) Chen, Z. H.; Lin, Y. M.; Rooks, M. J.; Avouris, P. *Phys. E* **2007**, *40*, 228–232.
- (8) Datta, S. S.; Strachan, D. R.; Khamis, S. M.; Johnson, A. T. C. *Nano Lett.* **2008**, *8*, 1912–1915.
- (9) Elias, A. L.; Botello-Mendez, A. R.; Meneses-Rodriguez, D.; Gonzalez, V. J.; Ramirez-Gonzalez, D.; Ci, L.; Munoz-Sandoval, E.; Ajayan, P. M.; Terrones, H.; Terrones, M. *Nano Lett.* **2010**, *10*, 366–372.
- (10) Kosynkin, D. V.; Higginbotham, A. L.; Sinitskii, A.; Lomeda, J. R.; Dimiev, A.; Price, B. K.; Tour, J. M. *Nature* **2009**, *458*, 872–876.
- (11) Wang, X. R.; Dai, H. J. *Nat. Chem.* **2010**, *2*, 661–665.
- (12) Cai, J. M.; Ruffieux, P.; Jaafar, R.; Bieri, M.; Braun, T.; Blankenburg, S.; Muoth, M.; Seitsonen, A. P.; Saleh, M.; Feng, X. L.; Mullen, K.; Fasel, R. *Nature* **2010**, *466*, 470–473.
- (13) Chen, Y. C.; de Oteyza, D. G.; Pedramrazi, Z.; Chen, C.; Fischer, F. R.; Crommie, M. F. *ACS Nano* **2013**, *7*, 6123–6128.
- (14) Cloke, R. R.; Marangoni, T.; Nguyen, G. D.; Joshi, T.; Rizzo, D. J.; Bronner, C.; Cao, T.; Louie, S. G.; Crommie, M. F.; Fischer, F. R. *J. Am. Chem. Soc.* **2015**, *137*, 8872–8875.
- (15) Durr, R. A.; Haberer, D.; Lee, Y. L.; Blackwell, R.; Kalayjian, A. M.; Marangoni, T.; Ihm, J.; Louie, S. G.; Fischer, F. R. *J. Am. Chem. Soc.* **2018**, *140*, 807–813.
- (16) Narita, A.; Feng, X. L.; Hernandez, Y.; Jensen, S. A.; Bonn, M.; Yang, H. F.; Verzhbitskiy, I. A.; Casiraghi, C.; Hansen, M. R.; Koch, A. H. R.; Fytas, G.; Ivasenko, O.; Li, B.; Mali, K. S.; Balandina, T.; Mahesh, S.; De Feyter, S.; Mullen, K. *Nat. Chem.* **2014**, *6*, 126–132.
- (17) Vo, T. H.; Shekhirev, M.; Lipatov, A.; Korlacki, R. A.; Sinitskii, A. *Faraday Discuss.* **2014**, *173*, 105–113.
- (18) Bennett, P. B.; Pedramrazi, Z.; Madani, A.; Chen, Y. C.; de Oteyza, D. G.; Chen, C.; Fischer, F. R.; Crommie, M. F.; Bokor, J. *Appl. Phys. Lett.* **2013**, *103*, 253114.
- (19) Llinas, J. P.; Fairbrother, A.; Barin, G. B.; Shi, W.; Lee, K.; Wu, S.; Choi, B. Y.; Braganzza, R.; Lear, J.; Kau, N.; Choi, W.; Chen, C.; Pedramrazi, Z.; Dumsclaff, T.; Narita, A.; Feng, X. L.; Mullen, K.; Fischer, F.; Zettl, A.; Ruffieux, P.; Yablonovitch, E.; Crommie, M.; Fasel, R.; Bokor, J. *Nat. Commun.* **2017**, *8*, 633.
- (20) Abbas, A. N.; Liu, G.; Narita, A.; Orosco, M.; Feng, X. L.; Mullen, K.; Zhou, C. W. *J. Am. Chem. Soc.* **2014**, *136*, 7555–7558.
- (21) Shekhirev, M.; Vo, T. H.; Kunkel, D. A.; Lipatov, A.; Enders, A.; Sinitskii, A. *RSC Adv.* **2017**, *7*, 54491–54499.
- (22) Blake, P.; Hill, E. W.; Castro Neto, A. H.; Novoselov, K. S.; Jiang, D.; Yang, R.; Booth, T. J.; Geim, A. K. *Appl. Phys. Lett.* **2007**, *91*, 063124.
- (23) Li, W.; Moon, S.; Wojcik, M.; Xu, K. *Nano Lett.* **2016**, *16*, 5027–5031.
- (24) Marangoni, T.; Haberer, D.; Rizzo, D. J.; Cloke, R. R.; Fischer, F. R. *Chem. - Eur. J.* **2016**, *22*, 13037–13040.
- (25) Vo, T. H.; Shekhirev, M.; Kunkel, D. A.; Morton, M. D.; Berglund, E.; Kong, L. M.; Wilson, P. M.; Dowben, P. A.; Enders, A.; Sinitskii, A. *Nat. Commun.* **2014**, *5*, 8.
- (26) Jiao, L. Y.; Wang, X. R.; Diankov, G.; Wang, H. L.; Dai, H. J. *Nat. Nanotechnol.* **2010**, *5*, 321–325.
- (27) Huang, B.; Babcock, H.; Zhuang, X. *Cell* **2010**, *143*, 1047–1058.
- (28) Sahl, S. J.; Hell, S. W.; Jakobs, S. *Nat. Rev. Mol. Cell Biol.* **2017**, *18*, 685–701.
- (29) Albertazzi, L.; van der Zwaag, D.; Leenders, C. M. A.; Fitzner, R.; van der Hofstad, R. W.; Meijer, E. W. *Science* **2014**, *344*, 491–495.
- (30) Berro, A. J.; Berglund, A. J.; Carmichael, P. T.; Kim, J. S.; Liddle, J. A. *ACS Nano* **2012**, *6*, 9496–9502.
- (31) Onogi, S.; Shigemitsu, H.; Yoshii, T.; Tanida, T.; Ikeda, M.; Kubota, R.; Hamachi, I. *Nat. Chem.* **2016**, *8*, 743–752.
- (32) Oracz, J.; Adolfsen, K.; Westphal, V.; Radzewicz, C.; Borgstrom, M. T.; Sahl, S. J.; Prinz, C. N.; Hell, S. W. *Nano Lett.* **2017**, *17*, 2652–2659.
- (33) Stohr, R. J.; Kolesov, R.; Xia, K. W.; Reuter, R.; Meijer, J.; Logvenov, G.; Wrachtrup, J. *ACS Nano* **2012**, *6*, 9175–9181.
- (34) Verzhbitskiy, I. A.; De Corato, M.; Ruini, A.; Molinari, E.; Narita, A.; Hu, Y.; Schwab, M. G.; Bruna, M.; Yoon, D.; Milana, S.; Feng, X.; Mullen, K.; Ferrari, A. C.; Casiraghi, C.; Prezzi, D. *Nano Lett.* **2016**, *16*, 3442–3447.
- (35) Lieber, E.; Rao, C. N. R.; Chao, T. S.; Hoffman, C. W. W. *Anal. Chem.* **1957**, *29*, 916–918.
- (36) Rust, M. J.; Bates, M.; Zhuang, X. W. *Nat. Methods* **2006**, *3*, 793–795.
- (37) Dertinger, T.; Colyer, R.; Iyer, G.; Weiss, S.; Enderlein, J. *Proc. Natl. Acad. Sci. U. S. A.* **2009**, *106*, 22287–22292.
- (38) Gustafsson, N.; Culley, S.; Ashdown, G.; Owen, D. M.; Pereira, P. M.; Henriques, R. *Nat. Commun.* **2016**, *7*, 12471.
- (39) Zschieschang, U.; Klauk, H.; Mueller, I. B.; Strudwick, A. J.; Hintermann, T.; Schwab, M. G.; Narita, A.; Feng, X. L.; Mullen, K.; Weitz, R. T. *Adv. Elec. Mater.* **2015**, *1*, 1400010.